10 Dynamics of Glaciers and Ice Sheets

10.1 RESPONSE TO CHANGES IN SURFACE MASS BALANCE

How glaciers react to a (sudden) change in surface mass balance is often described by the kinematic wave theory. In 1885, L. de Marchi was the first to suggest the existence of such waves on glaciers (Marchi, 1911), and the theory was further developed by Finsterwalder (1907). Half a century later, Weertman (1958) and Nye (1958) reintroduced kinematic waves to glaciology and showed how this theory applies to glaciers. In a series of papers, Nye (1961; 1963a, b, c; 1965a, b) developed this theory further. The following discussion is based largely on these papers.

A kinematic wave is described by the following equation:

$$\frac{\partial q}{\partial t} + c\,\frac{\partial q}{\partial x} = b,\tag{10.1}$$

in which q represents a volume flux, c the speed of the wave, and b a local production term. The term *kinematic wave* was introduced by Lighthill and Whitham (1955a, b), although equation (10.1) was derived some hundred years earlier to describe flood movement traveling downstream on long rivers (Boussinesq, 1877; Seddon, 1900). Another application of the theory is traffic flow on long, crowded roads (Lighthill and Whitham, 1955b). Kinematic waves are essentially different from dynamic waves such as waves on the ocean surface. Newton's equations of motion do not play a role in kinematic waves (other than, perhaps, by linking the wave speed to the volume flux), as they do for dynamic waves that exist because of the inertia terms in the equations of motion. At any location, the kinematic wave possesses only one wave velocity whereas dynamic waves are characterized by at least two velocities traveling in both directions relative to the medium in which the wave occurs. Glacier flow is sufficiently slow that inertia or acceleration terms may be neglected (which reduces Newton's second law to equilibrium of forces), so that dynamic waves do not occur on glaciers.

Kinematic waves owe their existence to conservation of volume or mass (in traffic flow, this would be the number of cars), when a relation exists between the discharge, concentration, and position. The starting point is the continuity equation (5.18) expressing conservation of ice mass, or volume, if the density is taken constant. To keep the analysis simple, one-dimensional flow along the x-axis is considered. The width of the glacier is taken constant, and the bed is horizontal. This means that the terminus of the glacier is on land, and calving tidewater glaciers are excluded from

the analysis. For an equilibrium glacier to exist, ablation near the terminus must be sufficiently large to compensate for accumulation in the upper regions of the glacier.

The continuity equation becomes

$$\frac{\partial H}{\partial t} + \frac{\partial (HU)}{\partial x} = M. \tag{10.2}$$

Assuming lamellar flow, the depth-averaged glacier speed is (Section 4.2)

$$U = -A_o H^{n+1} \left| \frac{\partial h}{\partial x} \right|^{n-1} \frac{\partial h}{\partial x}, \tag{10.3}$$

where

$$A_o = \frac{2A}{n+2} (\rho g)^n. \tag{10.4}$$

On a horizontal bed, the slope of the ice surface is equal to the thickness gradient. To simplify the notation,

$$\alpha = -\frac{\partial H}{\partial x}, \tag{10.5}$$

is used in the following analysis.

A reference or datum state is now defined, for example, the steady state of the glacier before the change in surface mass balance, with ice thickness H_o and ice flux $Q_o = H_o U_o$ (rather than considering the ice velocity, U, it is more convenient to consider the ice flux, Q = HU). The change in snowfall or ablation results in perturbations from this steady state. The perturbation in ice thickness, H_1 and ice flux, Q_1, are assumed to be small compared with the reference thickness and flux. This assumption allows the perturbation flux to be linearized using a series expansion

$$Q_1 = \left(\frac{\partial Q}{\partial H} \right)_o H_1 + \left(\frac{\partial Q}{\partial \alpha} \right)_o \alpha_1 =$$
$$= C_o H_1 + D_o \alpha_1, \tag{10.6}$$

where

$$C_o = (n+2) A_o H_o^{n+1} \alpha_o^n =$$
$$= (n+2) U_o, \tag{10.7}$$

and

$$D_o = n A_o H_o^{n+2} \alpha_o^{n-1} =$$
$$= \frac{n Q_o}{\alpha_o}. \tag{10.8}$$

These expressions are readily derived by writing $Q = HU$ and substituting equation (10.3) for the ice velocity.

The physical meaning of C_o and D_o can be understood by differentiating expression (10.6) for the perturbation flux with respect to time, giving

$$\frac{\partial Q_1}{\partial t} = C_o \frac{\partial H_1}{\partial t} - D_o \frac{\partial^2 H_1}{\partial x \partial t}. \tag{10.9}$$

The perturbation thickness can be eliminated from this equation by considering the continuity equation. The reference state satisfies continuity. Substituting $H = H_o + H_1$ and $Q = Q_o + Q_1$ for the total ice thickness and ice flux, respectively, into the continuity equation (10.2) and subtracting continuity for the reference state gives

$$\frac{\partial H_1}{\partial t} + \frac{\partial Q_1}{\partial x} = M_1, \tag{10.10}$$

as the continuity equation for the perturbation. In this expression, M_1 denotes the perturbation in surface accumulation. Using this equation to eliminate H_1 from equation (10.9) gives the following expression for the rate of change of Q_1

$$\frac{\partial Q_1}{\partial t} = C_o M_1 - C_o \frac{\partial Q_1}{\partial x} + D_o \frac{\partial^2 Q_1}{\partial x^2} + D_o \frac{\partial M_1}{\partial x}. \tag{10.11}$$

Comparing this expression with equation (10.1) shows that the perturbation is described by a kinematic wave equation. The first term on the right-hand side describes local production. The second term represents downstream advection of the kinematic wave, while the third term represents horizontal diffusion of the perturbation, with D_o the diffusivity. The speed at which the wave travels downglacier is C_o; from equation (10.7) it follows that the wave travels at about five times the reference ice velocity.

If the perturbation flux is eliminated from equation (10.10) by substituting (10.6), the following equation for H_1 is obtained:

$$\frac{\partial H_1}{\partial t} = -H_1 \frac{\partial C_o}{\partial x} - \left(C_o - \frac{\partial D_o}{\partial x} \right) \frac{\partial H_1}{\partial x} + D_o \frac{\partial^2 H_1}{\partial x^2} + M_1. \tag{10.12}$$

This equation can be solved for the perturbation thickness if C_o and D_o are known functions of distance along the flowline. As noted above, C_o is proportional to the ice velocity, U_o. The ice velocity increases over the accumulation area and is often largest in the middle regions of the glacier; in the ablation area, the velocity decreases, becoming small near the head and snout. A similar variation in C_o may be expected. Similarly, D_o may be expected to be of a form similar to the reference mass flux, that is, with a maximum in the middle part of the glacier. Based on these observations, Nye (1963b) adopts simple polynomial forms for these functions, namely,

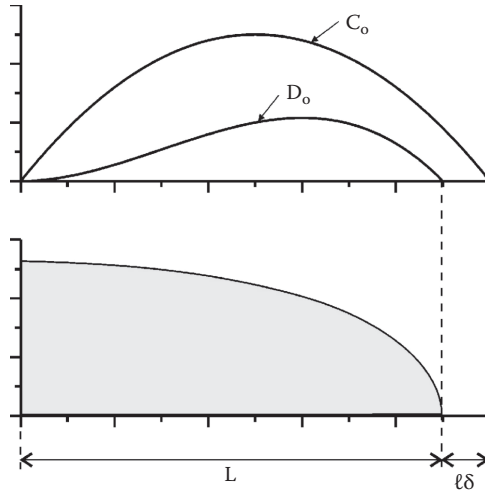$$C_o = \frac{x}{T_c} \left(1 - \frac{x}{\ell} \right), \tag{10.13}$$

FIGURE 10.1   Along-flow variation in kinematic wave velocity, C_o, and diffusivity, D_o, as given by equations (10.37) and (10.38). For clarity $\delta = 0.1$ instead of the much smaller actual value ~0.006.

and

$$D_o \;=\; \frac{E\,x^2}{T_c}\left(1 - \delta - \frac{x}{\ell}\right). \tag{10.14}$$

The length of the reference glacier is

$$L \;=\; \ell(1 - \delta). \tag{10.15}$$

The small quantity, $\delta \sim 0.006$, is introduced to prevent C_o from being zero at the snout of the glacier (Figure 10.1). The parameter T_c is a time scale, estimated by Nye (1963b) to be about 6 yr. The dimensionless parameter, E, is about 0.9 according to Nye (1963b). Substituting expressions (10.13) and (10.14) into equation (10.12) for the perturbation thickness, gives

$$\frac{\partial H_1}{\partial t} = \left(-\frac{1}{T_c} + \frac{x}{2T_c\,\ell}\right)H_1 \;-\; \left[\frac{x}{T_c}\left(1 - \frac{x}{\ell}\right) - \frac{E\,x}{2T_c}(1 - \delta) + \frac{E\,x^2}{3T_c\,\ell}\right]\frac{\partial H_1}{\partial x} \;+$$

$$+\; \frac{E\,x^2}{T_c}\left(1 - \delta - \frac{x}{\ell}\right)\frac{\partial^2 H_1}{\partial x^2} \;+\; M_1 \tag{10.16}$$

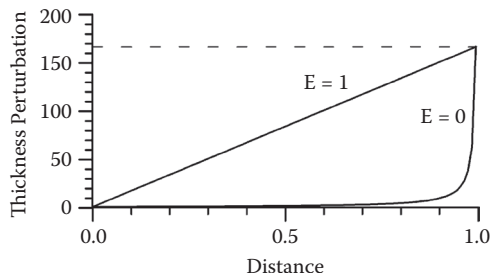if the perturbation in accumulation is constant along the glacier.

FIGURE 10.2 Change in ice thickness after a uniform stepwise increase in surface accumulation. The thickness perturbation is normalized by $M_1 T_c$, and the distance along the glacier by ℓ. For both solutions, $\delta = 0.006$. The solution for $E = 0$ corresponds to the case in which diffusion along the glacier is neglected.

An analytical solution can be found for a step-change in surface accumulation (or ablation, if M_1 is negative) that is constant along the glacier. For $E = 1$, the resulting change in ice thickness is

$$H_1(x) = M_1 T_c \left(1 + \frac{x}{\delta \ell}\right),\tag{10.17}$$

while for $E = 0$, the solution becomes

$$H_1(x) = M_1 T_c \left(1 - \frac{x}{\ell}\right)^{-1}.\tag{10.18}$$

For other values of E, the solution has to be determined numerically. For all values of E, the change in thickness at the upglacier boundary ($x = 0$) is equal to the perturbation in surface mass balance multiplied by the time scale T_c, while the change at the terminus equals $M_1 T_c / \delta$. A realistic value of E is about 1, and the thickness perturbation increases linearly with distance downglacier. If diffusion is neglected ($E = 0$), the thickness change is almost constant along most of the glacier and increases very rapidly near the terminus. In Figure 10.2 these two solutions are shown.

Adopting the value $E = 1$, the time-dependent solution can be found by first noting that the steady-state solution (10.17) is linear in x. Following Nye (1963b), the time-dependent solution is written as

$$H_1(x,t) = \sum_{k=0}^{K} b_k(t) x^k,\tag{10.19}$$

where the coefficients b_k are functions of time only. Substituting in equation (10.16) and equating the coefficients of like powers of x to zero (the equation must be satisfied for each value of x, which means that each coefficient must be zero) gives the solution

$$H_1(x,t) = M_1 T_c - M_1 T_c e^{-t/T_c} + M_1 T_c \left(\frac{1}{\delta} + \frac{2 e^{-t/T_c}}{1-2\delta} - \frac{e^{-2\delta t/T_c}}{\delta(1-2\delta)} \right) \frac{x}{\ell}. \quad (10.20)$$

This expression shows that there are two time scales, namely, T_c and $T_c/2\delta$. The first time scale is associated with the speed at which the kinematic wave travels downglacier, while the second, much longer time scale is related to diffusion. With $\delta = 0.006$ and $T_c = 6$ yr, the time scale for diffusion is about 500 yr. It is worthwhile to consider the time scale for adjustment in more detail, and in particular the long diffusion time scale. This requires a closer look at the terminus of the glacier.

For the geometry under consideration, with the snout of the glacier on land and subject to ablation, the ice flux at the terminus approaches zero, but the velocity should remain finite. This means that the velocity must become independent of the ice thickness (which approaches zero at the terminus), so that the ice flux becomes proportional to the ice thickness, rather than proportional to H^4. Denoting the speed at the terminus by U_e, the flux at the terminus is $Q_o(L) = H(L) U_e$, and

$$C_o(L) = U_e, \quad (10.21)$$

instead of equation (10.7). From parameterization (10.13) for C_o, its value at the terminus is

$$C_o(L) = \frac{\delta\ell}{T_c}, \quad (10.22)$$

if terms with δ^2 may be neglected. Combining these two expressions gives the time scale for diffusion

$$T_d = \frac{1}{2} \frac{\ell}{U_e}. \quad (10.23)$$

Since δ is small, ℓ may be replaced by the actual length of the glacier, L, and this equation can be written as

$$T_d = f \frac{L}{U_e}, \quad (10.24)$$

with $f = 0.5$ according to Nye's model.

The problem with the time scale predicted by equation (10.24) is that it depends critically on what happens near the snout of the glacier. Also, equation (10.24) suggests that small glaciers have response times of several hundred years, which does not seem to be supported by records of climate and glacier fluctuations. Jóhannesson

et al. (1989a) argue that the long time scale predicted by Nye's theory is the consequence of the assumed dynamics near the snout and the overestimation of the change in volume of the glacier after a sudden change in surface mass balance. Jóhannesson et al. (1989b) discuss this issue in more detail and show that the predicted changes in volume and speed at the terminus are highly sensitive to the choice of C_o and D_o along the glacier.

Van de Wal and Oerlemans (1995) use a numerical flow-band model to study propagation of kinematic waves on glaciers. According to their results, these waves travel at a speed of about 6 to 8 times the ice surface velocity. This compares favorably with the linear theory outlined above, which predicts a wave velocity of about five times the ice surface speed. Van de Wal and Oerlemans (1995) attribute the difference to the increasing gradient in ice velocity in the ablation zone. Using a realistic geometry (the Hintereisferner in Austria), the model predicts an increase of about 10% in the local ice velocity, depending on the position along the glacier and on the amplitude of the kinematic wave. Because of this moderate increase, kinematic waves are difficult to detect from measurements of ice velocity alone. Van de Wal and Oerlemans (1995) argue that synchronous changes in ice velocity on a glacier are not an indication of kinematic waves and that many of the observations of what have been classified as kinematic waves may in reality be manifestations of variations in basal sliding. In order to correctly identify kinematic waves on glaciers, time series of both ice velocity and surface elevation are needed because, in a kinematic wave, these two quantities are coupled.

The polynomial forms (10.13) and (10.14) proposed by Nye (1963b) apply to land-terminating glaciers with zero ice velocity at the terminus. For Greenland and Antarctic outlet glaciers this is not a realistic assumption. When considering flowlines extending from the interior to the grounding line, glacier speed is often observed to increase steadily. To accommodate these observations in the context of the kinematic wave theory, Van der Veen (2001) adopted an empirical approach. Using measurements of glacier speed and surface slope on Petermann Glacier in northwest Greenland, empirical parameterizations for the kinematic wave speed, C_o, and diffusivity, D_o, can be found through regression. Substituting these relations into the kinematic wave equation (10.12), glacier response to changes in surface mass balance can be evaluated by numerically integrating this equation forward in time. Figure 10.3 shows the calculated response of Petermann Glacier to a sudden and uniform increase in surface accumulation of 0.2 m/yr. To allow for comparison with Nye's solution, constant width of the glacier is assumed in this calculation. Initially, the glacier responds by thickening at a rate equal to the increase in surface accumulation. At the grounding line, the rate of thickness change decreases rapidly and a new equilibrium is established after a few hundred years. At the ice divide, 500 km inland from the grounding line, adjustment takes considerably longer and a new equilibrium is not established until after several thousands of years. The greatest thickening occurs at the ice divide. This result is opposite of the solution derived by Nye (1963b), which shows the greatest change in ice thickness at the terminus and no change at the divide (Figure 10.2). The reason for this contrasting response is that in the parameterization of glacier speed adopted by Nye, no mass is permitted to leave the glacier. The empirical velocity profile adopted by Van der Veen
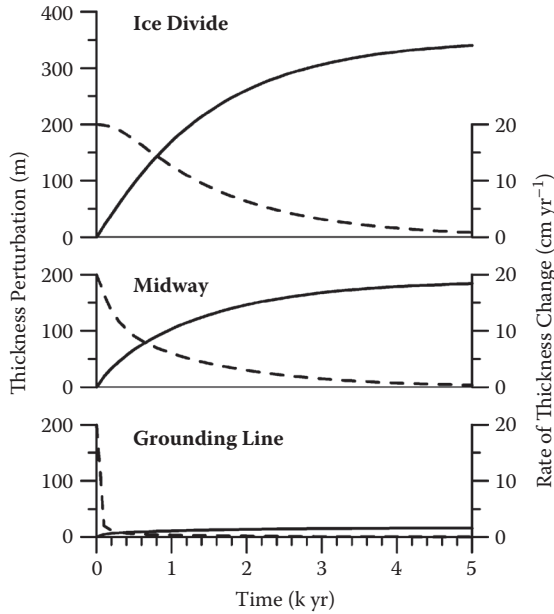
FIGURE 10.3 Ice sheet response to a uniform in surface accumulation (M = 0.2 m/yr). Constant width is assumed. The solid curves (scale on the left) show the thickness perturbation, and the dashed curves (scale on the right) show the rate of thickness change at three points along the 500 km long glacier. (From Van der Veen, C. J., *J. Geoph. Res.,* 106, 34047–34058, 2001. Copyright by the American Geophysical Union.)

(2001) allows part of the increased surface accumulation to be evacuated across the grounding line.

10.2   RESPONSE TO GROUNDING LINE THINNING

The kinematic wave theory discussed in Section 10.1 can also be applied to evaluate glacier response to imposed thinning at the grounding line. As shown by Alley and Whillans (1984), grounding-line thinning will be attenuated upglacier primarily through diffusion. Taking the diffusivity, D_o, constant along the glacier (as suggested by observations on Petermann Glacier; Van der Veen, 2001) and assuming constant flow-band width, the kinematic wave equation (10.12) simplifies to

$$\frac{\partial H}{\partial t} = D_o \frac{\partial^2 H}{\partial x^2}. \tag{10.25}$$

An analytical solution can be found following the similarity approach outlined by Turcotte and Schubert (2002, Section 4-15) for instantaneous heating or cooling of a semi-infinite half space. To simplify the analysis, the position of the grounding line is kept fixed at x = 0. This simplification is not as restrictive as it may appear to be.

Depending on the bed topography, thinning at the grounding line may result in retreat over some distance. In that case, the solution derived in this section applies to the part of the glacier upstream of the new grounding line position. The imposed thinning is then the change in ice thickness at this location.

To find a solution to the diffusion equation (10.25), thickness perturbations are normalized as

$$\hat{H}(x,t) = \frac{H(x,t)}{\Delta H(0)}, \tag{10.26}$$

where $\Delta H(0)$ represents the prescribed instantaneous thickness change at the grounding line at $t = 0$. This transformation does not change the form of the diffusion equation but simplifies the boundary conditions to

$$\hat{H}(x,0) = 0,$$

$$\hat{H}(0,t) = 1, \tag{10.27}$$

$$\hat{H}(\infty,t) = 0.$$

The diffusivity has dimension of (length)^2/time; thus the quantity $\sqrt{D_o\,t}$ has the dimension of length. This length scale may be considered a characteristic diffusion length and is used to define a nondimensional similarity variable as

$$\eta = \frac{x}{2\sqrt{D_o\,t}}. \tag{10.28}$$

The factor 2 is introduced to simplify the solution. Using formal similarity theory, it can be shown that the solution, $\hat{H}(x,t)$, is a function of η only.

To rewrite the diffusion equation in terms of derivatives with respect to η, the chain rule for differentiation has to be invoked. Considering first the term on the left-hand side of equation (10.25), this gives

$$\frac{\partial\hat{H}}{\partial t} = \frac{d\hat{H}}{d\eta}\frac{\partial\eta}{\partial t} = \frac{d\hat{H}}{d\eta}\left(-\frac{1}{2}\frac{\eta}{t}\right). \tag{10.29}$$

Similarly,

$$\frac{\partial\hat{H}}{\partial x} = \frac{d\hat{H}}{d\eta}\frac{\partial\eta}{\partial x} = \frac{d\hat{H}}{d\eta}\left(\frac{1}{2\sqrt{D_o\,t}}\right), \tag{10.30}$$

and the second derivative is

$$\frac{\partial^2\hat{H}}{\partial x^2} = \frac{\partial}{\partial x}\left[\frac{d\hat{H}}{d\eta}\left(\frac{1}{2\sqrt{D_o\,t}}\right)\right] = \frac{\partial}{\partial\eta}\left[\frac{d\hat{H}}{d\eta}\left(\frac{1}{2\sqrt{D_o\,t}}\right)\right]\frac{\partial\eta}{\partial x} = \frac{1}{4}\frac{1}{D_o\,t}\frac{d^2\hat{H}}{d\eta^2}. \tag{10.31}$$

Substituting these results in equation (10.25) gives

$$-\frac{1}{2}\frac{\eta}{t}\frac{d\hat{H}}{d\eta} = \frac{1}{4}\frac{1}{D_o t}\frac{d^2\hat{H}}{d\eta^2}D_o,$$ (10.32)

or

$$-\eta\frac{d\hat{H}}{d\eta} = \frac{1}{2}\frac{d^2\hat{H}}{d\eta^2}.$$ (10.33)

Note that introducing the similarity variable, η, has reduced the partial differential equation (10.25) to the ordinary differential equation (10.33) and that the three boundary conditions (10.27) are replaced by the following two:

$$\hat{H}(\infty) = 0,$$

$$\hat{H}(0) = 1.$$ (10.34)

To integrate equation (10.33), define

$$\phi = \frac{d\hat{H}}{d\eta}.$$ (10.35)

Substituting in equation (10.33) gives

$$-\eta\phi = \frac{1}{2}\frac{d\phi}{d\eta},$$ (10.36)

or

$$-\eta\, d\eta = \frac{1}{2}\frac{d\phi}{\phi}.$$ (10.37)

Integration yields

$$-\eta^2 = \ln\phi - \ln C_1,$$ (10.38)

where C_1 is an integration constant. This equation can be rewritten as

$$\phi = C_1 e^{-\eta^2}.$$ (10.39)

Recalling the definition (10.35) of ϕ, one more integration gives the nondimensional thickness perturbation

$$\hat{H}(\eta) = C_1 \int_0^\eta e^{-\bar{\eta}^2}\, d\bar{\eta} + C_2.$$ (10.40)

At the grounding line, $\eta = 0$ and $\hat{H}(0) = 1$, giving $C_2 = 1$. Using

$$\int_0^\infty e^{-\bar{\eta}^2} \, d\bar{\eta} = \frac{\sqrt{\pi}}{2}, \qquad (10.41)$$

applying the first boundary condition in (10.34), the other integration constant is found to be equal to $C_2 = -2/\sqrt{\pi}$.

Finally, the solution can be written as

$$\hat{H}(\eta) = 1 - \frac{2}{\sqrt{\pi}} \int_0^\eta e^{-\bar{\eta}^2} \, d\bar{\eta} = 1 - \mathrm{erf}(\eta) = \mathrm{erfc}(\eta). \qquad (10.42)$$

In this equation, $\mathrm{erf}(\eta)$ is the error function and $\mathrm{erfc}(\eta)$ the complimentary error function. Values for these functions can be calculated using standard numerical routines (for example, Press et al., 1992, p. 213).

The solution (10.42) allows thickness perturbations to be calculated for any combination of distance from the grounding line and time after thinning. Figure 10.4 shows how the wave of adjustment travels upglacier following sudden thinning at $x = 0$ and $t = 0$. Figures 10.5 and 10.6 illustrate how the time scale for adjustment increases
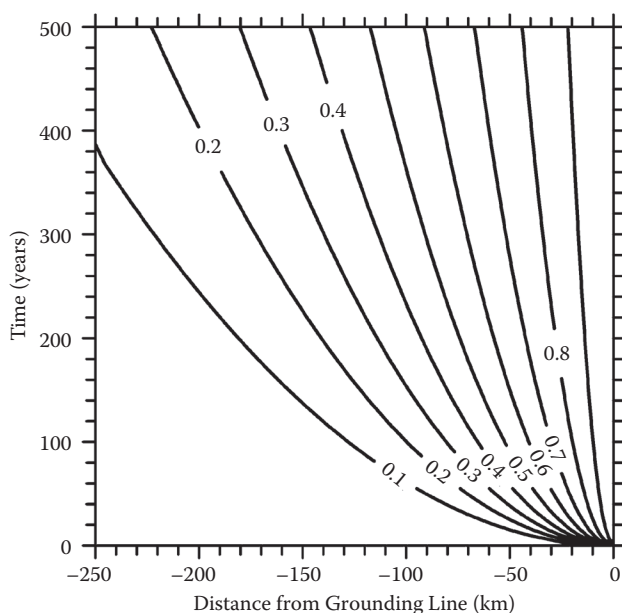

FIGURE 10.4 Transient glacier response to a sudden thinning at the grounding line at t = 0. Contours represent the thickness perturbation normalized by the imposed change at the grounding line. (From Van der Veen, C. J., *J. Geoph. Res.,* 106, 34047–34058, 2001. Copyright by the American Geophysical Union.)
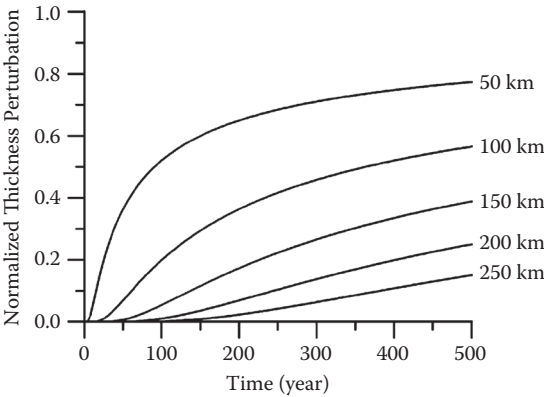
FIGURE 10.5 Normalized thickness perturbations at selected distance upstream of the grounding line after sudden thinning at the grounding line at t = 0. (From Van der Veen, C. J., *J. Geoph. Res.,* 106, 34047–34058, 2001. Copyright by the American Geophysical Union.)

rapidly in the upglacier direction. This is the direct consequence of the assumption that diffusion is the primary controlling process of glacier adjustment. For a diffusion equation such as equation (10.25), a time L^2/D_o is required for thickness perturbations to propagate upglacier over a distance L. This time scale is proportional to the square of the distance from the grounding line, and the speed at which the wave propagates inland decreases rapidly toward the interior. For Petermann Glacier, $D_o \approx 30 \times 10^6$ m^2/yr, giving a wave propagation speed of ~30 km/yr at the grounding line. At a distance of 100 km inland, this speed has decreased to ~300 m/yr (Van der Veen, 2001).
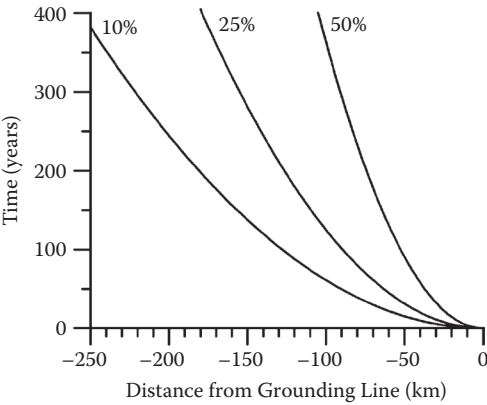

FIGURE 10.6 Time required for partial adjustment (labels indicate the amount of adjustment as a percentage of the equilibrium response) following sudden thinning at the grounding line at t = 0. (From Van der Veen, C. J., *J. Geoph. Res.,* 106, 34047–34058, 2001. Copyright by the American Geophysical Union.)

In the kinematic wave theory, response of an outlet glacier is described as a perturbation to a reference state. Possible feedback mechanisms that may lead to continued grounding-line retreat are not included in this theory. Feedback mechanisms that have been suggested as making marine terminating outlet glaciers unstable are discussed later in this chapter.

10.3 TIME-DEPENDENT SIMILARITY SOLUTIONS

In the previous section, similarity theory is applied to find analytical solutions describing how a sudden perturbation at the grounding line diffuses upglacier. The same methods can be used to find time-dependent exact analytical similarity solutions for the evolving profile of ice sheets. The first of such solutions applied to ice sheets are provided by Halfar (1981) for the case of two-dimensional flow along a flowline, and by Halfar (1983) for an axisymmetric ice cap. That solution was used by Nye (2000) to investigate the polar caps of Mars. Both the Halfar and Nye solutions apply to ice caps with zero surface accumulation. Bueler et al. (2005) expanded on these previous studies by allowing for nonzero accumulation. The motivation for these studies was primarily to provide a set of exact analytical time-dependent solutions that can serve as a tool for evaluating numerical ice-flow models. Bueler et al. (2005) note that "unfortunately the Halfar solution does not appear in the standard [glaciological] textbooks" (p. 291). The aim of this section is to remedy this deficiency.

Following Halfar (1983) and Nye (2000), an axisymmetric ice sheet on a horizontal bed and subject to zero surface accumulation is considered. In that case, the volume of the ice sheet is constant, and as the ice spreads out laterally, the thickness at the center decreases. The following derivation, based on Nye (2000), is somewhat lengthy, and readers not interested in the mathematical details can skip to the results.

The continuity equation for an axisymmetric ice sheet on a flat bed is derived in Section 5.4 and reads (with $M = 0$)

$$\frac{\partial H}{\partial t} = \frac{1}{r}\frac{\partial}{\partial r}\left[r\,A_o\,H^{n+2}\left|\frac{\partial H}{\partial r}\right|^{n-1}\frac{\partial H}{\partial r}\right], \tag{10.43}$$

where H represents the ice thickness and r the radial distance from the center. The radial ice flux, $Q(r, t)$, is given by

$$Q(r,t) = -A_o\,H^{n+2}\left|\frac{\partial H}{\partial r}\right|^{n-1}\frac{\partial H}{\partial r}, \tag{10.44}$$

and the continuity equation can also be written as

$$r\frac{\partial H}{\partial t} + \frac{\partial}{\partial r}(r\,Q) = 0. \tag{10.45}$$

Nye (2000) allows for depression of the initially flat bed by the weight of the ice (assuming equilibrium local isostatic adjustment), but for simplicity that effect is not included here.

As in Section 10.2 the ice thickness is nondimensionalized. For the case under consideration, an appropriate thickness scale is the thickness at the ice divide, $H_o(t)$. Then

$$\hat{H}(r,t) = \frac{H(r,t)}{H_o(t)}. \tag{10.46}$$

Similarly, if $R(t)$ denotes the radius of the ice sheet, a scaled radial coordinate is defined as

$$\hat{r} = \frac{r}{R(t)}. \tag{10.47}$$

The assumption is now made that the scaled ice thickness is a function of $\hat{r}$ only, independent of time, t, and $\hat{H}(r,t) = \hat{H}(r)$. This means that the scaled shape of the ice sheet keeps the same analytical form. However, because both the thickness at the divide and the radius of the ice sheet are allowed to change over time, the aspect ratio of the ice sheet, H/R, will change.

With these definitions, the first term on the left-hand side of the continuity equation (10.45) becomes

$$r\frac{\partial H}{\partial t} = r\frac{\partial}{\partial t}(H_o \hat{H}) = r\hat{H}\frac{dH_o}{dt} + rH_o\frac{d\hat{H}}{d\hat{r}}\frac{d\hat{r}}{dt}. \tag{10.48}$$

The term involving the change in scaled radius with time can be eliminated by considering that the volume of the ice sheet must remain constant (zero surface mass balance). This volume is proportional to $H_o R^2$ and thus

$$\frac{d}{dt}(H_o R^2) = R^2\frac{dH_o}{dt} + H_o 2R\frac{dR}{dt} = 0, \tag{10.49}$$

from which it follows that

$$\frac{dR}{dt} = -\frac{R}{2H_o}\frac{dH_o}{dt}. \tag{10.50}$$

This gives

$$\frac{d\hat{r}}{dt} = \frac{d}{dt}\left(\frac{r}{R}\right) = -\frac{r}{R^2}\frac{dR}{dt} =$$

$$= \frac{r}{2RH_o}\frac{dH_o}{dt} = \frac{\hat{r}}{2H_o}\frac{dH_o}{dt}. \tag{10.51}$$

Substituting this expression in equation (10.48) gives

$$r\frac{\partial H}{\partial t} = r\hat{H}\frac{dH_o}{dt} + r\frac{d\hat{H}}{d\hat{r}}\frac{\hat{r}}{2}\frac{dH_o}{dt} =$$

$$= R\hat{r}\frac{dH_o}{dt}\left[\hat{H} + \frac{\hat{r}}{2}\frac{d\hat{H}}{d\hat{r}}\right] = \frac{R}{2}\frac{dH_o}{dt}\frac{d}{d\hat{r}}\left(\hat{r}^2\,\hat{H}\right). \tag{10.52}$$

The flux term in the continuity equation (10.45) can be rewritten as

$$\frac{\partial}{\partial r}(Qr) = \frac{d}{d\hat{r}}(QR\hat{r})\frac{d\hat{r}}{dr} = \frac{d}{d\hat{r}}(Q\hat{r}). \tag{10.53}$$

The continuity equation can now be written in terms of the normalized radial distance as

$$\frac{R}{2}\frac{dH_o}{dt}\frac{d}{d\hat{r}}(\hat{r}^2\,\hat{H}) + \frac{d}{d\hat{r}}(Q\hat{r}) = 0. \tag{10.54}$$

Integrating this equation with respect to $\hat{r}$ at constant t gives

$$\frac{R}{2}\frac{dH_o}{dt}(\hat{r}^2\,\hat{H}) + (Q\hat{r}) = G(t), \tag{10.55}$$

where G(t) is a function of time, t, only. The radial ice flux is then

$$Q = \frac{G}{\hat{r}} - \frac{1}{2}R\hat{r}\hat{H}\frac{dH_o}{dt}. \tag{10.56}$$

At the ice divide, $\hat{r} = 0$, and Q = 0 at all times. This boundary condition can only be satisfied if G(t) = 0.

For lamellar flow, the ice flux is also given by equation (10.44), which can be written in terms of normalized variables as

$$Q = A_o H^{n+2}\left(-\frac{\partial H}{\partial r}\right)^n = A_o \hat{H}^{n+2} H_o^{n+2}\left[\frac{d}{d\hat{r}}\left(-\hat{H}H_o\right)\frac{d\hat{r}}{dr}\right]^n =$$

$$= A_o \hat{H}^{n+2} H_o^{n+2} H_o^n\left[-\frac{d\hat{H}}{d\hat{r}}\frac{1}{R}\right]^n = A_o \hat{H}^{n+2} H_o^{2n+2}\frac{1}{R^n}\left[-\frac{d\hat{H}}{d\hat{r}}\right]^n. \tag{10.57}$$

Equating both expressions for the ice flux gives

$$-\frac{1}{2}R\hat{r}\hat{H}\frac{dH_o}{dt} = A_o \hat{H}^{n+2} H_o^{2n+2}\frac{1}{R^n}\left[-\frac{d\hat{H}}{d\hat{r}}\right]^n, \tag{10.58}$$

and, after rearranging,

$$2\,A_o \frac{\hat{H}^{n+1}}{\hat{r}} \left[-\frac{d\hat{H}}{d\hat{r}} \right]^n = -\frac{R^{n+1}}{H_o^{2n+2}} \frac{dH_o}{dt}.$$

(10.59)

Now recall that the assumption is made that the scaled thickness, $\hat{H}$, is a function of the scaled radial distance, $\hat{r}$, only and independent of time. This means that both sides of equation (10.59) must be constant, say, equal to K. The thickness distribution can then be found by integrating the left-hand side with respect to $\hat{r}$, and the time dependence is obtained by integrating the right-hand side with respect to t.

Consider first the left-hand side of equation (10.59):

$$2\,A_o \frac{\hat{H}^{n+1}}{\hat{r}} \left[-\frac{d\hat{H}}{d\hat{r}} \right]^n = K,$$

(10.60)

or

$$-\hat{H}^{1+1/n}\,d\hat{H} = \left(\frac{K}{2\,A_o} \right)^{1/n} \hat{r}^{1/n}\,d\hat{r}.$$

(10.61)

This equation can be integrated to give

$$-\frac{n}{2n+1}\hat{H}^{2+1/n} = \left(\frac{K}{2\,A_o} \right)^{1/n} \frac{n}{n+1}\hat{r}^{1+1/n} + C.$$

(10.62)

By definition, at the ice divide ($\hat{r} = 0$), the scaled ice thickness must equal unity, and $\hat{H}(0,t) = 0$, giving $C = -n/(2n+1)$ for the integration constant. The second boundary condition is that the ice thickness is zero at the ice margin ($\hat{r} = 1$), and

$$K = 2\,A_o \left(\frac{n+1}{2n+1} \right)^n.$$

(10.63)

The scaled thickness distribution can now be written as (Halfar, 1983; Nye, 2000)

$$\hat{H}^{2+1/n} + \hat{r}^{1+1/n} = 1.$$

(10.64)

Note the similarity between this profile and the steady-state profile derived in Section 5.4.

To find an expression for the time-dependent divide thickness, $H_o(t)$, the right-hand side of equation (10.59) is considered. At $t = 0$, the divide thickness equals $\tilde{H}_o$ and the ice sheet radius is $\tilde{R}$. The requirement that the ice volume remains constant then implies

$$H_o(t)R^2(t) = \tilde{H}_o \tilde{R}^2,$$

(10.65)

which can be used to eliminate R(t) from the right-hand side of equation (10.59). This gives

$$H_o^{-5(n+1)/2} \frac{dH_o}{dt} = -\left(\tilde{R}^2 \tilde{H}_o\right)^{-(n+1)/2} K. \tag{10.66}$$

Noting that the right-hand side is constant, integration yields

$$-\frac{2}{5n+3} H_o^{-(5n+3)/2} = -(\tilde{R}^2 \tilde{H}_o)^{-(n+1)/2} K t + C. \tag{10.67}$$

The integration constant follows from the initial boundary condition that $H_o(t) = \tilde{H}_o$ and is given by

$$C = -\frac{2}{5n+3} \tilde{H}_o^{-(5n+3)/2}. \tag{10.68}$$

With K given by expression (10.63), the solution for the thickness at the ice divide can now be written as

$$H_o(t) = \tilde{H}_o \left(1 + \frac{t}{T}\right)^{-2/(5n+3)}, \tag{10.69}$$

with

$$T = \frac{1}{(5n+3) A_o} \left(\frac{2n+1}{n+1}\right)^n \frac{\tilde{R}^{n+1}}{\tilde{H}_o^{2n+1}}. \tag{10.70}$$

Finally, the change in radius follows from equation (10.65) and is given by

$$R(t) = \tilde{R} \left(1 + \frac{t}{T}\right)^{1/(5n+3)}. \tag{10.71}$$

To summarize the preceding derivation, equation (10.64) gives the normalized ice-sheet profile as a function of normalized radial distance. Ice thickness is scaled with the thickness at the ice divide, and distance is scaled with the radius of the ice sheet. As the ice spreads out, the divide thickness decreases according to equation (10.69) and the radius increases as described by equation (10.71).

Figure 10.7 shows how the divide thickness decreases with time, and Figure 10.8 shows how the radius increases (using $n = 3$ for the flow law exponent). The greatest rates of change occur at the start ($t = 0$); as time progresses, the rate of adjustment decreases. The reason for this is that the aspect ratio (height-to-width ratio) diminishes according to (from equations (10.69) and (10.71))

$$\frac{H_o(t)}{R(t)} = \frac{\tilde{H}_o}{\tilde{R}} \left(1 + \frac{t}{T}\right)^{-3/(5n+3)}. \tag{10.72}$$
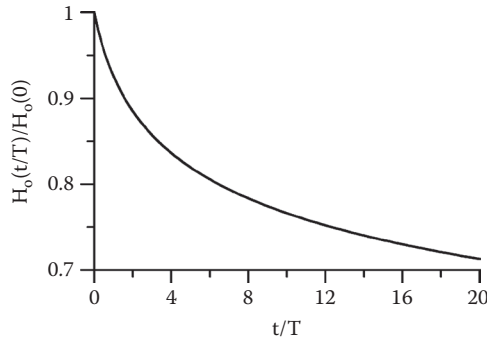
FIGURE 10.7 Decrease in ice thickness at the divide for the case of zero surface accumulation.

Thus, the slope of the ice surface decreases over time, resulting in slower ice speeds. Corresponding ice-sheet profiles are shown in Figure 10.9. Note that in this figure, the ice thickness is normalized by $\tilde{H}_o$ and the radial distance by $\tilde{R}$, instead of using equations (10.46) and (10.47). The reason for this is that these equations define the normalized thickness to vary from 1 at the divide to 0 at the margin, while the normalized radius increases from 0 to 1. Thus, the shape of the normalized profile (10.64) does not change over time.

The time scale for adjustment, T, is given by equation (10.70), with the constant, A_o, related to the rate factor, A, in Glen's flow law as (Section 5.3)

$$A_o = \frac{2A}{n+2}(\rho g)^n. \tag{10.73}$$

Thus, the time scale depends on the temperature of the ice and on the initial divide thickness and radius. For ice close to the melting temperature, $A \approx 10^{-7}$ kPa^{-3} yr^{-1}. Taking $\tilde{H}_o = 2$ km and $\tilde{R} = 500$ km for the initial geometry (at t = 0), the time scale is about 5000 years.
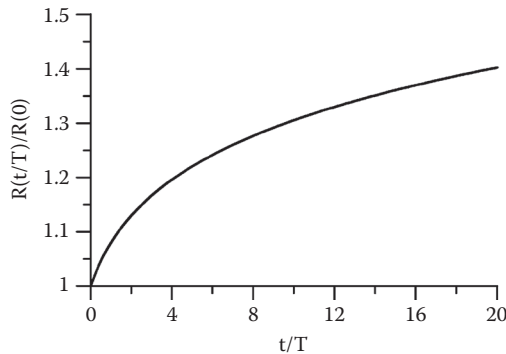
FIGURE 10.8 Increase in ice-sheet radius for the case of zero surface accumulation.
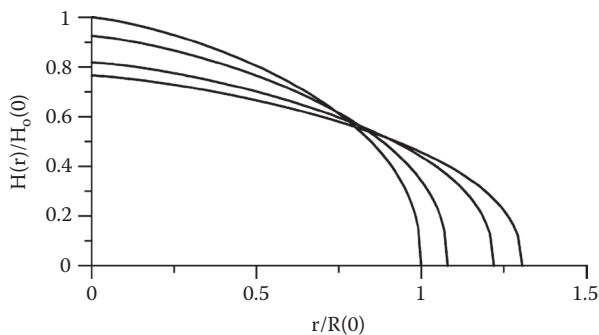
FIGURE 10.9 Surface profiles of an axisymmetric ice sheet for the case of zero surface accumulation, at times $t = 0$, $t = T$, $t = 5T$, and $t = 10T$. Note that the thickness is nondimensionalized by the divide thickness at $t = 0$, and the radial distance is nondimensionalized by the ice-sheet radius at $t = 0$.

As noted at the beginning of this section, Bueler et al. (2005) present similarity solutions corresponding to nonzero surface accumulation. Accumulation, M, is taken proportional to ice thickness and inversely proportional to time, such that

$$M = \frac{\lambda}{t} H, \tag{10.74}$$

with λ a constant parameter. Omitting the derivation here, the resulting ice-sheet profile is given by

$$H_\lambda(r,t) = \tilde{H}_o \left(\frac{t}{T}\right)^{-\alpha} \left[1 - \left(\left(\frac{t}{T}\right)^{-\beta} \frac{r}{\tilde{R}} \right)^{n/(2n+1)} \right]^{n/(2n+1)}, \tag{10.75}$$

where

$$\alpha = \frac{2 - (n+1)\lambda}{5n + 3}, $$

$$\beta = \frac{1 + (2n+1)\lambda}{5n + 3}. \tag{10.76}$$

The thickness at the divide changes with time as

$$H_o(t) = \tilde{H}_o \left(\frac{t}{T}\right)^{-\alpha}, \tag{10.77}$$

while the time evolution of the radius is given by

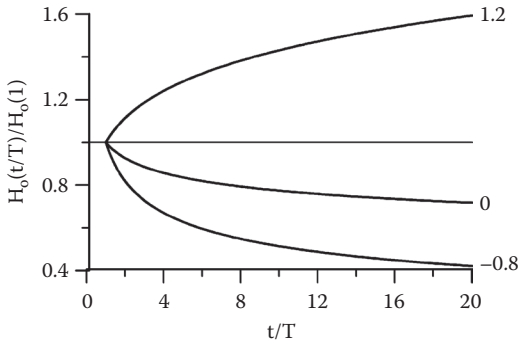$$R(t) = \tilde{R} \left(\frac{t}{T}\right)^{\beta}, \tag{10.78}$$

FIGURE 10.10 Change in ice thickness at the divide for three values of the accumulation parameter (indicated by the labels). $\lambda = 1.2$ corresponds to height-dependent accumulation, $\lambda = 0$ corresponds to zero surface accumulation, and $\lambda = -0.8$ corresponds to height-dependent ablation. In these solutions, $t = T$ corresponds to the initial profile.

(Bueler et al., 2005). In these solutions, the time, t, is defined somewhat different from the earlier solutions, and the initial time corresponds to $t = T$, as opposed to $t = 0$ as in the Halfar–Nye solution.

Figure 10.10 shows the change in ice thickness at the divide for three values of the accumulation parameter. The curve corresponding to $\lambda = 0$ is equivalent to the solution shown in Figure 10.7. The other two curves represent solutions for positive accumulation and for ablation. The corresponding change in radius is shown in Figure 10.11, while Figure 10.12 shows corresponding ice-sheet profiles at select times.

Bueler et al. (2005) propose a suite of tests for numerical ice-sheet models based on these exact, time-dependent analytical solutions. They proceed to test one numerical model and find that their explicit finite-difference scheme recovers the time-dependent
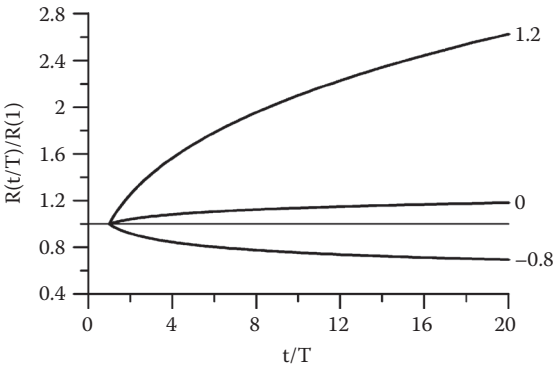

FIGURE 10.11 Change in ice-sheet radius for three values of the accumulation parameter (indicated by the labels). $\lambda = 1.2$ corresponds to height-dependent accumulation, $\lambda = 0$ corresponds to zero surface accumulation, and $\lambda = -0.8$ corresponds to height-dependent ablation. In these solutions, $t = T$ corresponds to the initial profile.
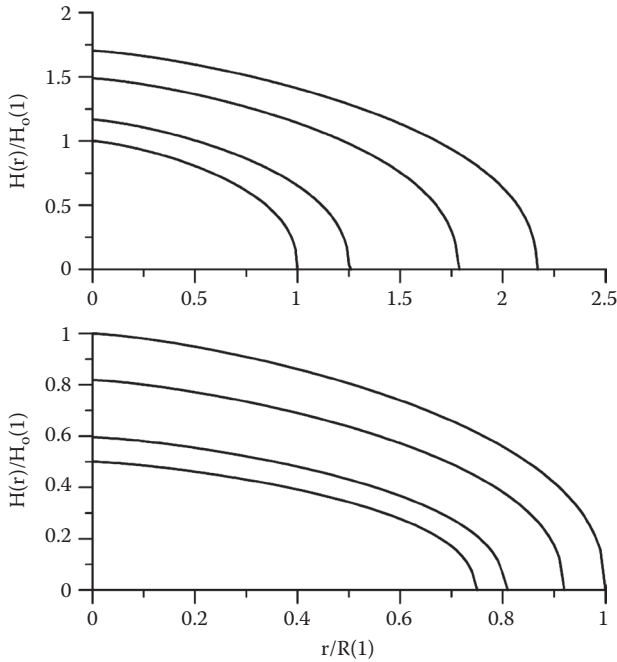
FIGURE 10.12 Surface profiles of an axisymmetric ice sheet for the case of height-dependent accumulation (top panel; $\lambda = 1.2$) and height-dependent ablation (bottom panel; $\lambda = -0.8$), at times $t = T$, $t = 2T$, $t = 6T$, and $t = 11T$. In these solutions, $t = T$ corresponds to the initial profile. The thickness is nondimensionalized by the divide thickness at $t = T$, and the radial distance is nondimensionalized by the ice-sheet radius at $t = T$.

analytical solutions. Rutt et al. (2009) compare the Glimmer community ice-sheet model against three of the time-dependent analytical solutions provided by Bueler et al. (2005) and find that, generally, model solutions converge toward the analytical solutions as the grid spacing and time step are decreased. Bueler et al. (2007) provide exact solutions to the thermomechanically coupled lamellar flow approximation in three spatial dimensions, but these are not similarity solutions. Sargent and Fastook (2010) construct manufactured analytical solutions for time-dependent and steady-state Stokes flow, both for two-dimensional flow along a flowline and for three-dimensional ice-sheet flow. Leng et al. (2012b) also derive solutions for three-dimensional, isothermal, nonlinear Stokes flow and use these to verify the parallel, high-order accurate, finite element, nonlinear Stokes ice-sheet model of Leng et al. (2012a). Results of this comparison show excellent agreement.

10.4 GLACIER SURGES

A glacier surge is a short period of comparatively fast motion following an extended period of normal flow. Meier and Post (1969) argue that the first and foremost characteristic that distinguishes surging glaciers is the fact that surges occur repeatedly.

This periodicity suggests that the longitudinal profile of a surging glacier is not stable. During the quiescent phase, which for a single glacier is fairly constant (of the order of 10 to 100 years), the ice speeds are generally small and the glacier thickens, most notably in the upper regions of the area affected by the surge. When the glacier reaches a certain thickness, a threshold may be reached and the ice speed increases by a factor of 10 or more and ice is rapidly drained from the upglacier area to the terminus. As a result, the thickness decreases rapidly in the upglacial regions, while near the terminus the thickness increases and the front may advance over several kilometers. This active phase, commonly referred to as the surge, is relatively short (months to a few years) compared with the quiescent phase. It is not clear what causes the surge to terminate, other than stating the obvious that conditions that allow the rapid flow cannot be maintained for prolonged periods of time, perhaps because the thickness of the glacier decreases rapidly during the surge.

One of the few glaciers that have been studied through several complete surge cycles is Medvezhiy Glacier located in the West Pamir Mountains in the Central Asian Republic of Tajikistan. The period of surges is 10 to 14 years, with surges having occurred in 1937, 1951, 1963, and 1973 (Dolgoushin and Osipova, 1975, 1978). Medvezhiy Glacier covers an area of about 25 km^2. Its large accumulation area is situated at an elevation of 4600 to 5500 m above sea level; the ablation area is nourished by a steep icefall and terminates at an elevation of 2840 m (during maximum advance) to 3000 m (during maximum retreat) above sea level. The surges are confined to the ice tongue below the ice fall. This tongue is about 8 km long and 100 to 200 m thick, and located in a narrow valley. The profiles before and after the 1963 surge are shown in the upper panel of Figure 10.13. Comparison of these profiles clearly shows that a considerable mass of ice was transferred from the upper part to the terminus, which is one of the characteristics of a glacier surge. In April 1963, the glacier snout started to advance, traveling a distance of 1600 m in a period of about two months. The increase in ice thickness in the lower part reached 150 m, while the surface in the upper part was lowered by up to 100 m. During the surge, the average ice speed was about 40 m/day, but a maximum of 100 m/day was reached during a two-week period apparently associated with the formation of a large horizontal fracture. After the surge, the terminal region became almost stagnant as the ice velocity decreased to a few cm per day. In the quiescent phase following the 1963 surge, the ice tongue consisted of two parts, namely, a zone of active ice, and the terminal inactive zone (Figure 10.13, middle panel). Because there was almost no flow of ice from the upper zone into the inactive zone, the mass balance of the inactive region was strongly negative and the thickness decreased steadily. In the active zone, the mass balance was positive due to inflow of ice from the accumulation area of the glacier. As this active lobe built up, it slowly expanded downglacier until a threshold was reached, and the next surge occurred in 1973 (Figure 10.13, lower panel).

A detailed record of changes in ice velocity during a surge is available for Variegated Glacier, Alaska. This glacier, with a length of ~20 km and located near Yakutat, Alaska, surged seven times during the 20th century with an average time between initiation of surges of 15 years (Lawson, 1997; Eisen et al., 2001). Eisen et al. (2001) found that a surge occurs when the cumulative mass balance reaches a threshold value and the time interval between successive surges depends on the
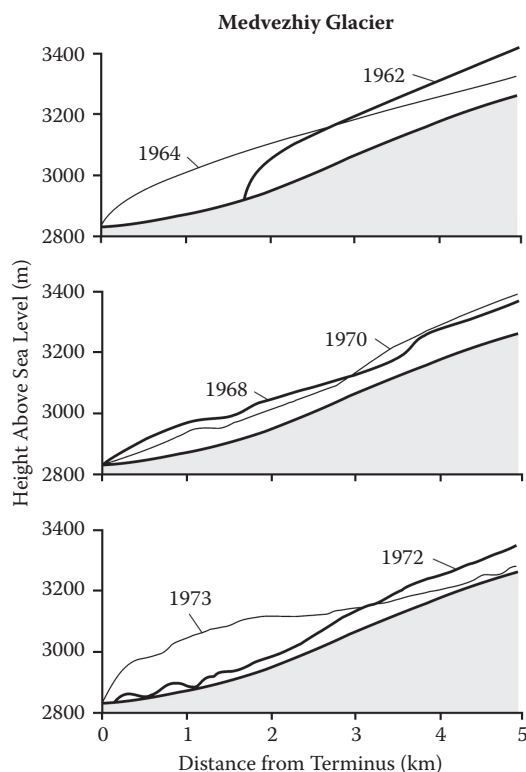
FIGURE 10.13   Longitudinal profiles of Medvezhiy Glacier, before and after the surges in 1963 and 1973. (After Dolgoushin, L. D., and G. B. Osipova, *Mater. Glyatsiologischeskikh Issled. Khronika. Obsuzhdeniya,* 32, 260–265, 1978.)

annual accumulation over that interval. The last recorded surge occurred in 1995 and was relatively small compared with earlier surges. This surge was initiated in the winter and terminated after two days of record high temperatures early in the following melt season (Eisen et al., 2005).

In 1973 a monitoring program was initiated to study the buildup of Variegated Glacier and the ensuing surge (Kamb et al., 1985; Raymond and Harrison, 1988). Between September 1973, and September 1981, the glacier thickened by as much as 60 m in the upper regions (about 60% of the total glacier length), while thinning occurred in the lower 40% of the glacier, up to about 40 m near the terminus. At the same time, the ice velocity increased in the upper region, while the terminus remained essentially stagnant. The boundary between the regions of net thickening and thinning slowly migrated downglacier at a speed of 0.3 km/yr. The location of maximum thickening rate appeared to propagate downglacier at a similar speed (Raymond and Harrison, 1988). The surge started in January 1982, with the velocity in the upper regions increasing from 2.6 to 9.2 m/day from late May to late June, and reaching a maximum of 10.4 m/day on June 26 (Kamb et al., 1985). Within a

few hours after the occurrence of the peak, the velocity dropped to less than 5 m/day and steadily decreased to about 1 m/day by mid-August. During this slowing down, five major pulses of velocity occurred, during which the peak velocity reached 3–7 m/day. By the end of September 1982, it appeared that the surge had ended. This phase of the surge was restricted to the upper region of the glacier, and the lower parts remained unaffected by the increase and subsequent decrease in velocity. In October 1982, the velocity in the upper region started to increase again, leveling off at 5–7 m/day in January 1983. After a sudden drop in early February 1983, the velocity gradually increased, reaching a maximum of about 15 m/day in mid-June. During this second phase, the surge propagated into the lower regions of the glacier, and the ice velocity there rose from less than 0.2 m/day in early May to 40–60 m/day in June. The surge terminated on July 4, when the velocity along the entire length of the glacier dropped dramatically over the course of a few hours (Kamb et al., 1985). Figure 10.14 illustrates how the surge front propagated downglacier. Ahead of the
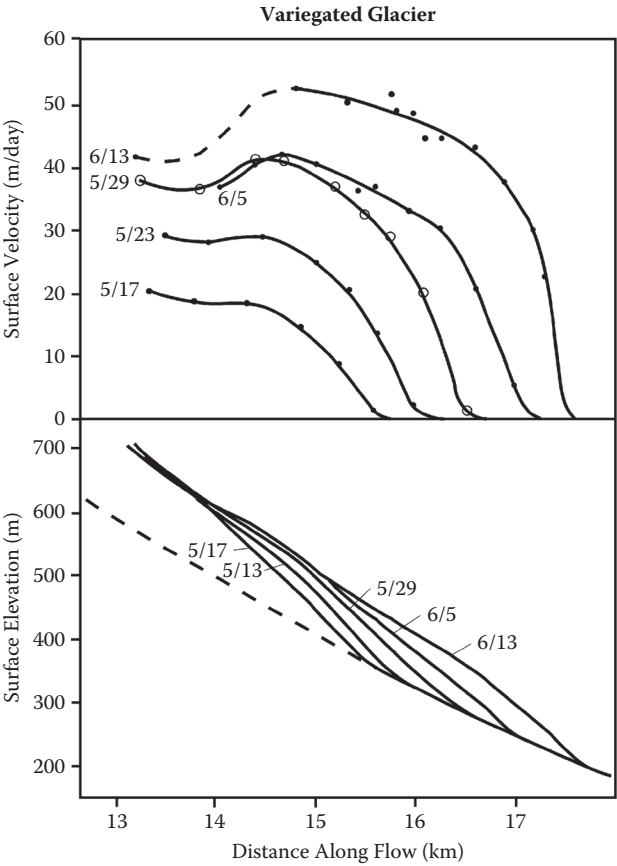

FIGURE 10.14 Propagation of the surge front on Variegated Glacier during May and June 1983. (From Kamb, B. et al., *Science,* 227, 469–479, 1985. Copyright 1985 by the American Association for the Advancement of Science.)

front, the ice was virtually stagnant, while the front advanced at an almost constant rate of 80 m/day. This rapid advance of the surge front, at a speed that exceeds the actual ice velocity, suggests that this advance is similar to a kinematic wave traveling along the glacier (Kamb et al., 1985).

It has long been recognized that surges are achieved by a switch in the basal conditions, allowing transition from slow to rapid flow. Initially, this transition was thought to be from a frozen glacier sole to a water-lubricated base, allowing rapid basal sliding. However, surges also occur in temperate glaciers such as Variegated Glacier, whose base remains well lubricated during the quiescent phase. This means that the no-sliding to sliding transition cannot explain why surges occur in these glaciers. Furthermore, a distinction needs to be made between glaciers resting on a hard and nondeformable bed and glaciers that rest on soft material. In view of the wide range of possible basal conditions, it is probably illusory to expect one theory of surges to apply to all glaciers. Nevertheless, a qualitative description can be given, based on the model presented by Fowler (1987b). This model is based on static external conditions, and in particular, changes in water input (seasonal or from individual rain events) are not included.

There are essentially two possibilities for the subglacial drainage system, namely, a system of Röthlisberger channels (Röthlisberger, 1972), or a linked-cavity system (Kamb, 1987). It could be argued that drainage in a water film at the bed represents a third possibility, but it is unlikely that such a film is of uniform thickness. Rather, one may expect the film to be thicker in some places, and almost pinched out in others. If so, there appears to be little difference between the water film and the linked-cavity system, and it may not be necessary to explicitly consider drainage through a film. The essential feature that allows transition from "slow" basal sliding to "rapid" basal sliding is the difference in water pressure in each of the drainage systems. Together with the assumption that the sliding speed is a function of this water pressure, it can be shown how the switch from one drainage system to the other leads to a surge.

In an R-channel, the effective pressure increases as the water flux through the channel increases (Röthlisberger, 1972; c.f. Section 7.5)

$$N_r \sim Q_w^{1/p}, \tag{10.79}$$

where $p \approx 12$. The effective pressure, N, is defined as the difference between the ice overburden pressure and the water pressure in the channel. Thus, the water pressure, P_w, decreases as the water flux, Q_w, increases. This means that water will tend to collect in the larger tunnels, and an arterial network of subglacial channels will develop with smaller channels feeding into larger tunnels. In a linked-cavity system, on the other hand, the water pressure increases as the water flux increases, and there is no tendency for water to collect in larger passageways. Provided that the sliding velocity is high and the water pressure not too large, a complicated network of meandering links that connect the cavities will remain stable (Kamb, 1987). Fowler (1987a) argues that for such a network to be able to discharge a reasonable amount of meltwater, some of the intercavity connections must enlarge to form small R-channels.

In that case, the effective pressure in the linked-cavity system is much smaller than that in an R-channel carrying the same water flux. That is

$$N_c = \delta N_r, \tag{10.80}$$

where N_r represents the effective pressure in an R-channel (equation (10.79)). The quantity δ depends on the degree of cavitation and the fraction of the bed that is free from cavities. For a typical glacier, δ may be 0.25 or smaller (Fowler, 1987b).

If the sliding velocity becomes sufficiently small, dissipational heat generated by the water flowing through a linked-cavity system is insufficient to maintain melting needed to counteract creep closure, and the drainage system may collapse into a tunnel system. On the other hand, if the sliding velocity becomes too large, a tunnel system will become unstable and a system of cavities connected by small channels will develop. Without going into the mathematical details, it can be shown (Fowler, 1987a) that the stability parameter, S, is a function of the ice velocity and the effective pressure

$$S \sim \frac{U}{N^n}, \tag{10.81}$$

where n = 3 represents the exponent in Glen's flow law for glacier ice. If S is smaller than some critical value, S_c, a tunnel system is stable and the effective basal pressure is large. But for $S > S_c$, the tunnel system collapses into a linked-cavity system, with (much) smaller effective pressure. This dependence is schematically illustrated in Figure 10.15, which shows the effective pressure, N, as a function of the stability parameter, S. The transition at $S = S_c$ may not be as sharp as shown in this figure, but for the present qualitative discussion, the picture shown in Figure 10.15 suffices. It may be noted that the implicit assumption is made here that the transition from tunnel to linked cavities occurs at the same critical value, S_c, as the transition from linked cavities to tunnels. This may not be true (Fowler, 1987a), but it is not clear whether introducing a hysteresis loop will significantly alter the qualitative aspects of the model.
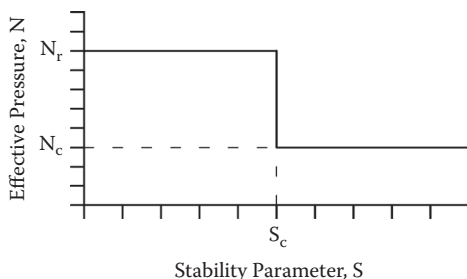

FIGURE 10.15 Schematic illustration of the dependency of the stability parameter, S, on the effective basal pressure, N. For small values of S, subglacial drainage is through tunnels, and the effective pressure is relatively large. For large values of S, drainage is through a linked-cavity system, with lower effective pressure.

Rather than considering how the effective pressure depends on the stability parameter, S, it is more instructive to consider how N depends on the sliding velocity, U. From the stability analysis summarized above, it follows that there are two critical velocities, namely,

$$U_1 \sim S_c N_r^n, \tag{10.82}$$

and

$$U_2 \sim S_c N_c^n. \tag{10.83}$$

For $U < U_1$ the tunnel system is stable and the effective pressure is equal to N_r, while for $U > U_2$, a linked-cavity system is stable and $N = N_c$. However, because the effective pressure in a tunnel is larger than that in a linked-cavity system, U_2 is smaller than U_1, and a range of velocities exists for which both drainage systems are possible. This is schematically illustrated in Figure 10.16, which shows the effective pressure as a function of the sliding velocity. To understand how this multivalued function leads to surging behavior, the sliding relation needs to be invoked.

While a universally applicable sliding relation has not yet been established, it is generally accepted that the sliding speed depends on basal drag and effective water pressure as in the generalized Weertman relation (c.f. Section 7.2)

$$U \sim \frac{\tau_b^m}{N^k}. \tag{10.84}$$

Using the functional relation between effective pressure and sliding speed shown in Figure 10.16, this sliding relation can be schematically represented by the curve shown in Figure 10.17. To adopt Fowler's (1987b) terminology, this curve is characterized by a "slow" branch and a "fast" branch.

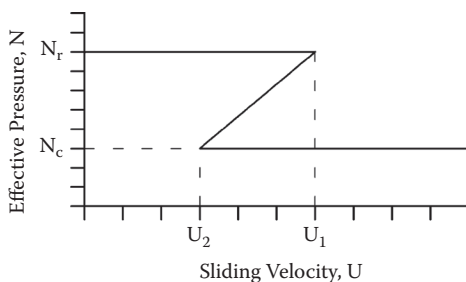
FIGURE 10.16 Schematic illustration between sliding velocity, U, and effective basal pressure, N. For sliding speeds smaller than U_1, a tunnel system with relatively large basal pressure is stable, while for $U > U_2$, the linked-cavity system with lower effective pressure is stable. Because $U2 < U_1$, there is a range of sliding velocities for which both drainage systems are possible.
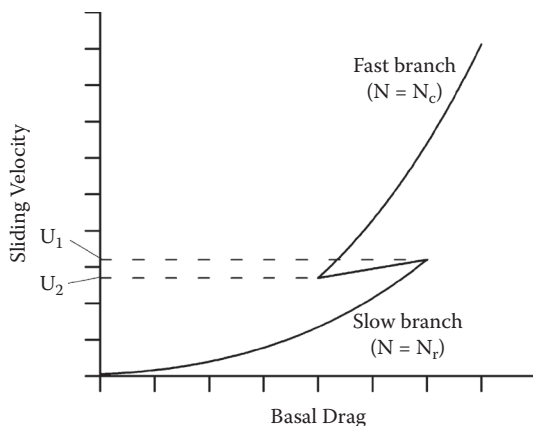
FIGURE 10.17   Schematic illustration of the relationship between sliding velocity and basal drag. The sliding relation is characterized by a slow and a fast branch. The coexistence of two possible sliding velocities for the same basal drag can lead to surge cycles.

Referring to Figure 10.18, a surge cycle can now be described. During the quiescent phase, the glacier builds up and its thickness increases, resulting in a larger driving stress. Making the reasonable assumption that the driving stress is primarily balanced by basal drag, the drag at the glacier bed gradually increases until a critical value is reached (point A in Figure 10.18). The sliding velocity has now become too large for subglacial tunnels to be maintained, and a linked-cavity system develops. As a result of the lower effective pressure, the ice velocity increases (point B). However, the (local) increase in mass discharge results in a loss of ice and a decrease in driving stress (and hence, basal drag). Thus, the sliding velocity decreases until sliding is too slow to maintain a linked-cavity system (point C). The cavities collapse and a tunnel system reforms, bringing the glacier in the slow-flow regime again (point D).

There are many factors that determine whether or not a particular glacier will exhibit surge-type behavior. First, surface accumulation must be large enough to allow the glacier to grow to the transition point A. If the steady-state size of the glacier is such that this point is never reached, the glacier will not switch to the fast-flow regime. Second, basal conditions must be such that the change in effective pressure (as described by the factor δ in equation (10.80)) is large enough. Generally, this requires a rough bed (Fowler, 1987b). Third, the difference between the two critical velocities, U_1 and U_2 (Figure 10.16), must be sufficiently large.

The model developed by Fowler (1987b) and outlined above applies only to glaciers whose bed is at the pressure melting temperature along most of the glacier length. This requirement does not apply to all surging glaciers. For example, Trapridge Glacier in the Yukon Territory, Canada, is a small (~4 km long) polythermal surge-type glacier resting on a bed of unconsolidated sediments (Clarke and Blake, 1991). The basal ice reaches the melting point only in the central area where the thickness is greatest. Near the terminus and the head of the glacier, the bed is
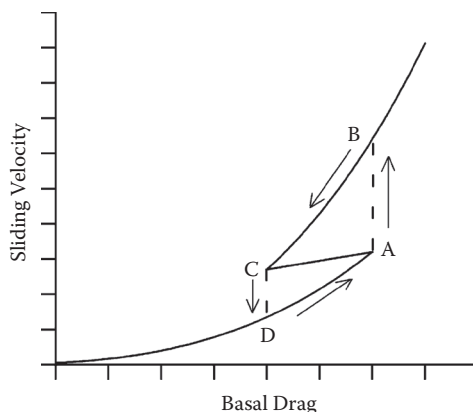
FIGURE 10.18   Schematic illustration of a complete surge cycle. See text for a description.

frozen and advance of the surge front appears to be associated with migration of the warm/cold boundary (Clarke, 1976; Clarke et al., 1984). Fowler et al. (2001) present a heuristic model for cyclic surging of such polythermal glaciers, with subglacial hydrology controlling both the flow of the glacier and deformation of subglacial till. The model produces oscillations (surges) if the permeability of unfrozen till is sufficiently small to impede water drainage and if the thickness of the till layer is small. Under those conditions, drainage of basal meltwater is restricted, resulting in higher water pressures and reduced effective basal pressure. At this stage, water is stored in "blisters," but eventually, discharge from these blisters becomes large enough to lower basal water pressure. Murray et al. (2003) argue that this model applies to the typical surge cycle of glaciers on Svalbard.

10.5   MARINE INSTABILITY

Many glaciologists have argued that, because of its marine nature, the West Antarctic Ice Sheet is inherently unstable and may respond drastically to (moderate) changes in climate (for example, Bentley, 1984; Hughes, 1973; Mercer, 1968, 1978; Thomas, 1979; Thomas and Bentley, 1978; Thomas et al., 1979; Weertman, 1974). This view is based on the idea that the large floating ice shelves that surround the grounded portion of this ice sheet regulate the discharge of inland ice. The grounding line tends to be unstable if the water depth is greater than some critical depth and the sea floor slopes downward toward the ice-sheet interior (as is the case in West Antarctica), and a reduction in size or complete removal of the ice shelves would initiate grounding-line retreat that may be irreversible and result in the collapse of the entire ice sheet.

Most of the West Antarctic Ice Sheet is grounded on a former sea floor, and currently the bed under the ice is well below sea level. A direct consequence of this is that the ice sheet is surrounded by floating ice shelves (indicated by dark shading in Figure 10.19). As the ice flows outward to the sea, its thickness decreases and, because the bed is below sea level, a point is reached where the weight of the ice becomes less than the upward buoyancy force of the sea water and the ice starts
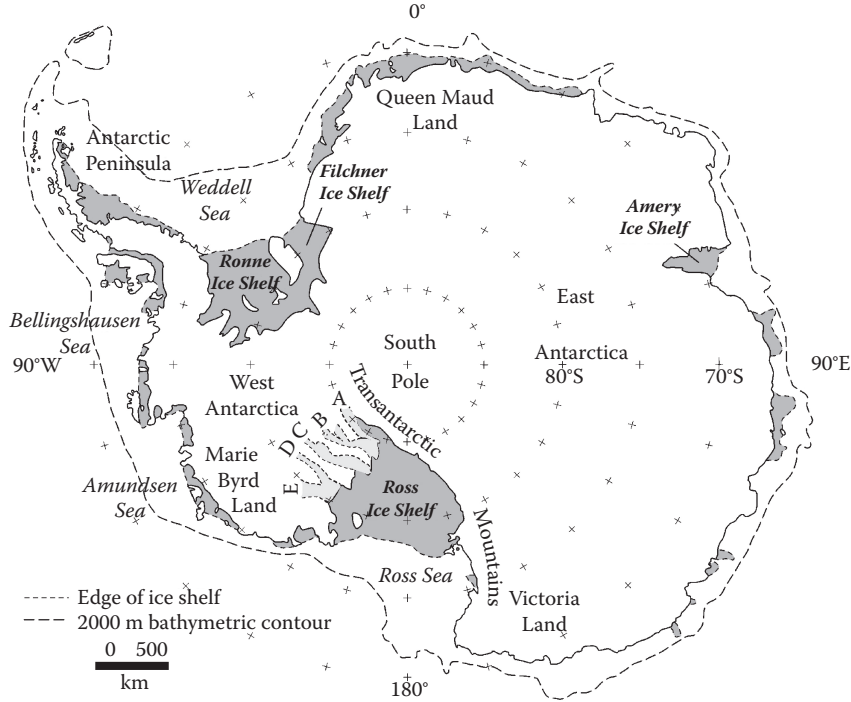
FIGURE 10.19   Location map of Antarctica. Dark shading represents the major ice shelves and light shading represents the five ice streams (labeled A–E; in 2001 these were renamed Mercer, Whillans, Kamb, Bindschadler, and MacAyeal Ice Streams, respectively) draining into the Ross Ice Shelf.

to float, forming an ice shelf. The boundary between grounded ice and floating ice shelves is called the *grounding line*. As shown in Figure 10.19, West Antarctica is almost completely surrounded by floating ice shelves, while smaller ice shelves are also found in East Antarctica. Ice shelves and floating ice tongues comprise about 57% of the Antarctic coast line. These ice shelves are nourished by ice streams and outlet glaciers, and by local accumulation. Mass loss occurs at the terminus where ice breaks off to form icebergs, and by basal melting.

Before discussing stability of the grounding line, it is instructive to have a closer look at the nature of the grounding zone and how different mapping methods have grounding-line positions that may differ by up to ~60 km (Brunt et al., 2010). Figure 10.20 shows a schematic view across the grounding zone. The line labeled G denotes the position of the actual grounding line, where the ice starts to float. This position can be determined accurately only through ground-based surveys such as radio-echo sounding or seismic methods (Brunt et al., 2010). Because this is impractical to do on a large scale, most reported grounding-line positions are based on the locations of one or more of the other surface features of the grounding zone. Vertical movements primarily associated with tides result in periodic
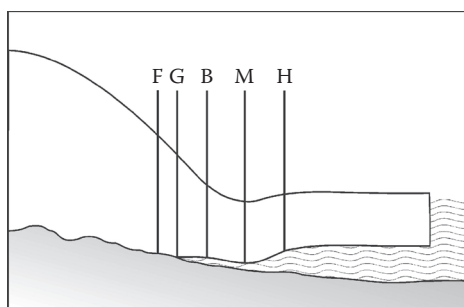
FIGURE 10.20 Schematic cross-section of the grounding zone showing the inland position of tidal flexure (F), the grounding line (G), the break in slope (B), the local minimum in surface elevation (M), and the hydrostatic point (H) where ice is in hydrostatic equilibrium. The grounding zone is defined as the region between points F and H. (From Brunt, K. M. et al., *Ann. Glaciol.,* 51(55), 71–79, 2010. Reprinted from the *Annals of Glaciology* with permission of the International Glaciological Society and the authors.)

vertical motions of the grounded ice. Point F corresponds to the landward limit of tidal flexure, and this position was used by Rignot (1998) to map the hinge line of Petermann Glacier in northwest Greenland. On the seaward end, the hydrostatic point H is the location where the ice shelf is in hydrostatic equilibrium with the ice shelf. The region between points F and H defines the grounding zone (Fricker et al., 2009; Brunt et al., 2010). In the grounding zone, there often is a local topographic minimum (point M in Figure 10.20) as well as one or more breaks in the surface slope (point B). Fricker et al. (2009, Table 1) discuss how different satellite sensors can be used to find different combinations of the features in the grounding zone. For comparison of grounding-line positions reported in different studies, it is thus important to make sure the same features are compared. Brunt et al. (2010) propose that the limit of tidal flexure (point F) is the most robust proxy for the location of the grounding line. On the other hand, for mass flux calculations into ice shelves, the location of point H is required because this represents the most upstream location where ice thickness can be estimated from the ice surface elevation and the flotation assumption (Brunt et al., 2010).

Mercer (1968, 1978) proposed that ice shelves are sensitive to moderate climate changes and cannot maintain their integrity once summer temperature or the annual mean temperature exceeds some threshold. Analysis of data on atmospheric warming and retreat of ice shelves surrounding the Antarctic Peninsula appears to confirm the existence of a thermal limit on ice-shelf viability (Vaughan and Doake, 1996). The observed pattern of ice-shelf retreat is consistent with a southward migration of the –5°C annual mean air temperature isotherm. Mercer (1968, 1978) further suggested that the peripheral ice shelves play a major buttressing role for discharge of inland ice, and their breakup would greatly enhance the discharge from the interior and could lead to the rapid collapse of the West Antarctic Ice Sheet.

The fringing ice shelves hypothesis summarized above is based on the observation that most of the ice shelves surrounding West Antarctica have formed in

embayments and are locally in contact with the seabed. Resistance from the lateral walls and ice rises obstructs the flow of the ice shelves, and the spreading rate is significantly smaller than would be observed if the shelves were spreading freely. This effect is often described by the back pressure, defined as the downglacial integrated resistance to flow associated with lateral drag and resistance from ice rises (Section 4.5). For an ice shelf spreading in one direction only, the back pressure at any point on the ice shelf is calculated from

$$\sigma_b(x) \;=\; \frac{1}{H} \int_x^L \frac{H\tau_s}{W}\, d\bar{x}, \tag{10.85}$$

where τ_s represents the shear stress at the margins, W denotes the half width of the ice shelf and $x = L$ represents the position of the ice-shelf front (with the x-axis along the direction of flow). This back pressure reduces the spreading rate as compared with that of a free-spreading ice shelf. That is

$$\dot{\varepsilon}_{xx} \;=\; \theta \left(\frac{R_{xx}^{(0)} - \sigma_b}{B} \right)^n, \tag{10.86}$$

in which B and n represent the flow law parameters and θ accounts for transverse spreading (c.f. Section 4.5; for an ice shelf spreading in the x-direction only, $\theta = 2^{-n}$). In equation (10.86), $R_{xx}^{(0)}$ represents the stretching stress for a free-floating ice shelf on which the driving stress is balanced entirely by gradients in longitudinal stress. As derived in Section 4.5, this stress is given by

$$R_{xx}^{(0)} \;=\; \frac{\rho g}{2} \left(1 - \frac{\rho}{\rho_w} \right) H, \tag{10.87}$$

with ρ_w the density of sea water.

   If the back pressure is zero and the ice shelf is spreading freely in one direction, the stretching rate is proportional to the nth power of the ice thickness

$$\dot{\varepsilon}_{xx} \;=\; \left[\frac{\rho g}{4B} \left(1 - \frac{\rho}{\rho_w} \right) \right]^n H^n. \tag{10.88}$$

This solution was derived first by Weertman (1957b) and represents the maximum spreading rate of an ice shelf of thickness H. The effect of lateral drag and ice rises is to reduce this spreading rate through the back pressure. Thus, if the back pressure decreases, due to thinning of the ice shelves (which reduces lateral drag and may result in the ungrounding of pinning points) or due to a shortening of the shelf (which reduces the length over which lateral drag acts), the creep rate for a given ice thickness increases.

How the creep rate affects thickness change can be seen by considering the continuity equation (Section 5.2). Considering flow in the x-direction only, this equation reads

$$\frac{\partial H}{\partial t} = -\frac{\partial (HU)}{\partial x} + M =$$

$$= -U\frac{\partial H}{\partial x} - H\frac{\partial U}{\partial x} + M. \qquad (10.89)$$

Replacing the along-flow velocity gradient by the stretching rate (equation (10.86)) and using expression (10.87) for the stretching stress, gives

$$\frac{\partial H}{\partial t} = -U\frac{\partial H}{\partial x} - H\left(\frac{CH - \sigma_b}{2B}\right)^n + M, \qquad (10.90)$$

with

$$C = \frac{\rho g}{2}\left(1 - \frac{\rho}{\rho_w}\right). \qquad (10.91)$$

While this equation is derived from ice-shelf dynamics, it can also be applied to the grounding line, where the flow regime changes from ice-stream flow to ice-shelf spreading. Thus, the thickness at the grounding line is affected by three factors, namely, advection from upglacier (first term on the right-hand side), creep thinning (second term), and local accumulation or ablation, M. If these three terms sum to zero, the thickness at the grounding line does not change and the position of the grounding line is stationary. However, changing any of the three terms on the right-hand side of equation (10.90) results in a thickness change, which could initiate irreversible grounding-line retreat if feedback processes become important.

According to the second term on the right-hand side of equation (10.90), creep thinning at the grounding line depends strongly on the ice thickness, H. This dependency leads to an important feedback between creep thinning and seabed topography, as illustrated in Figure 10.21. Consider first the situation in which the seafloor slopes downward toward the exterior (left panel). If the grounding line advances, for example, because advection from upglacier increases, the thickness at the grounding line increases, leading to larger creep thinning, which slows the rate of advance. Similarly, if the grounding line retreats, creep thinning decreases, thus retarding the rate of retreat. So, for the geometry shown in the left panel, the interaction between creep thinning and ice thickness provides a negative feedback, slowing the rate of both advance and retreat. However, the situation shown in the panel on the right, with the seabed sloping downward toward the interior, is more representative of West Antarctica. Now the feedback is positive and an advance of the grounding line leads to a decrease in creep thinning, allowing the grounding line to advance further, while a retreat results in increased creep thinning and accelerated retreat.

The presence of a restricted ice shelf may have a stabilizing effect on grounding-line retreat or advance. At present, the calving fronts of the ice shelves are mostly
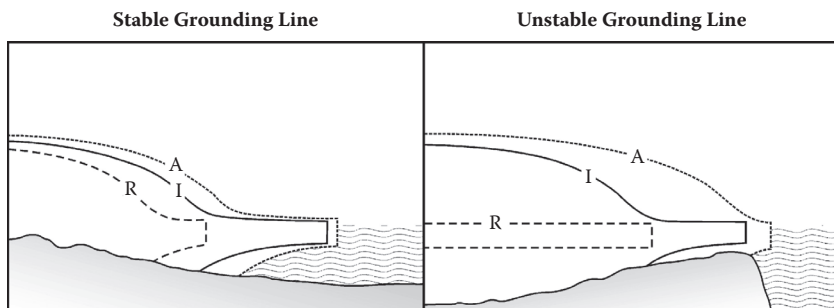
Stable Grounding Line   Unstable Grounding Line

FIGURE 10.21 Interaction between grounding-line migration and basal topography. The panel on the left represents a stable configuration with the bed sloping downward from the ice-sheet interior. The panel on the right represents an unstable situation. Profiles labeled I represent the initial geometry, and profiles labeled A and R represent the geometry after advance and retreat, respectively. (From Thomas, R. H., *J. Glaciol.,* 24, 167–177, 1979. Reprinted from the *Journal of Glaciology* with permission of the International Glaciological Society and the author.)

at the end of the confining embayments, so an advance of the grounding line results in a shorter shelf length over which lateral drag acts. Thus, from equation (10.85), an advancing grounding line reduces the back pressure at the grounding line, which results in larger creep thinning, slowing the rate of advance. Similarly, retreat of the grounding line increases the back pressure, which slows the retreat. If the ice shelf becomes sufficiently large, the position of the grounding line may stabilize.

The model for studying grounding-line migration described above was developed by Thomas (1977) and applied to the Holocene retreat of the West Antarctic Ice Sheet by Thomas and Bentley (1978) and by Thomas (1985) to estimate the contribution of the polar ice sheets to rising sea level after a climatic warming. The main difficulty in these applications is to account for changes in advection from upglacier (the first term on the right-hand side of equation (10.90)) as the grounding line migrates. Thomas and Bentley (1978) calculate this term based on the assumption that the inland ice-sheet profile is parabolic, which allows the change in ice-sheet volume (and hence the discharge across the grounding line) to be calculated for a given change in grounding-line position. Thomas (1985) makes the assumption that a transition zone exists upstream from the grounding line. In this zone, the stretching rate is assumed constant (equal to the value calculated from equation (10.86)). With the velocity at the head of this transition zone known, the speed at the grounding line can be calculated from the stretching rate and the length of the transition zone. As the grounding line migrates, Thomas (1985) makes the additional assumption that both the length of the transition zone and the speed at the upglacial end of this zone remain constant. While the various assumptions that have been used affect the quantitative results, the qualitative behavior is the same, and these studies indicate that the West Antarctic Ice Sheet is unstable with respect to changes at the grounding line. In view of the model formulation, this result should come as no surprise.

The main objection against the instability model discussed above is the inconsistency in incorporating ice-shelf dynamics. Creep thinning is calculated from an

expression based on ice-shelf dynamics, but the velocity at the grounding line or at the head of the transition zone is not affected by the presence of the ice shelf. Thus, an increase in stretching rate (due to a decrease in back pressure) leads to larger creep thinning but has no immediate effect on the ice speed. However, all strain rates affect this velocity through the effective strain rate, and an increase in stretching rate may be expected to result in an increase in speed at the grounding line as well. By not including this effect, the model becomes inherently unstable and prohibits a stable ice-sheet response to changes at the grounding line.

The inherent difficulty in modeling marine ice sheets appears to be how to merge the distinctly different flow regimes present in the system. On the grounded part in the interior, flow is dominated by vertical shear and can be described by the lamellar flow model. On floating ice shelves, basal drag is absent and the driving stress is balanced by gradients in longitudinal stress and by lateral drag. Coupling these flow regimes is a transition zone of unknown length. Despite some 40 years of theoretical and numerical modeling, debate continues about the nature of this flow transition and consequences for ice-sheet stability.

The first theoretical treatment of the stability of a grounding line is the study of Weertman (1974), who considered a two-dimensional ice sheet on a bed below sea level with initially constant slope. Bedrock adjustment to the ice load is included by assuming local isostatic equilibrium (equation (9.85)). By deriving an expression for the ice flux across the grounding line, steady-state grounding-line positions can be found by comparing the ice flux across the grounding line with integrated upglacier accumulation. The argument is that a small advance of the grounding line increases the size of the ice sheet and thus increases total accumulation over the grounded portion. If the downward slope of the bed at the grounding line is not large enough, the increase in total accumulation exceeds the increase in ice flux across the grounding line, and the ice sheet will continue to grow until the edge of the continental shelf is reached. Weertman's results show that an ice sheet that rests on a bed that was flat before isostatic adjustment and below sea level is inherently unstable. Depending on how deep the bed is below sea level, a small perturbation in grounding-line position (for example, resulting from a change in sea level) will cause continued retreat and the ice sheet will disappear entirely, or the grounding line will advance to the edge of the continental shelf. If the bed slopes away from the divide (as in the left panel of Figure 10.21), a stable ice sheet is possible.

An updated analysis of grounding-line stability can be found in Schoof (2007a, b; 2011), who applied a boundary layer theory to derive an expression for the ice flux across the grounding line. A more simple derivation of this flux is provided by Hindmarsh (2012, Appendix B). Weertman-type sliding is assumed with basal drag related to the sliding speed as in equation (7.9); that is

$$\tau_b = C_s |U|^{1/m-1} U. \tag{10.92}$$

Neglecting gradients in longitudinal stress and lateral drag, force balance reduces to a balance between driving stress and basal drag, and

$$C_s |U|^{1/m-1} U = -\rho g H \frac{\partial h}{\partial x}. \tag{10.93}$$

The second equation to consider is the continuity equation (10.90). Setting the back stress, σ_b, to zero, and assuming steady state, this equation becomes

$$U\frac{\partial H}{\partial x} + H\left(\frac{CH}{2B}\right)^n = M. \tag{10.94}$$

At the grounding line, the ice becomes afloat and the surface elevation is related to the ice thickness through hydrostatic equilibrium (equation (4.55)) and

$$h = \left(1 - \frac{\rho}{\rho_w}\right)H. \tag{10.95}$$

Using this relation to eliminate the thickness gradient from equations (10.93) and (10.94) gives the ice flux across the grounding line

$$Q = \left[\frac{2C^{n+1}}{C_s\left(2B\right)^n}\right]H^{(n+m+3)/(m+1)}. \tag{10.96}$$

More formal derivations, based on asymptotic expansions for the flow in boundary layers, are presented in a series of papers by C. Schoof. Flow of the ice sheet is described by the shallow ice approximation (or lamellar flow model), while interactions at the grounding line are represented through two boundary conditions that constrain the ice thickness at the grounding line (from flotation) and the ice flux across the grounding line as a function of local water depth (Schoof, 2007a, 2011, 2012). Applying a linear stability analysis, Schoof (2012) confirmed earlier inferences based on mass-balance arguments (Weertman, 1974; Schoof, 2007a, b) that the stability of equilibrium grounding-line positions is determined by the balance between discharge flux across the grounding line and total upglacier accumulation.

It could be argued that the sliding relation (10.93) adopted by Schoof is unrealistic because it does not account for the effect of basal pressure on the sliding speed. The more commonly used sliding relation (7.25) results in basal drag tending to zero toward the grounding line as the effective basal pressure approaches zero as the ice reaches floatation. Assuming that this lowered basal drag is compensated by lateral drag, a derivation similar to that above shows that the ice flux across the grounding line is proportional to H^{n+1} (Hindmarsh, 2012, equation (16)). Thus, for this case similar reasoning can be applied to show that grounding lines can be stable only where the bed slopes downward sufficiently steeply.

The crucial assumptions in these analytical models are that the peripheral ice shelf is unconfined and that gradients in longitudinal stress (termed *membrane stresses* by Hindmarsh, 2009) are unimportant in the balance of forces at the grounding line. This is valid when considering possible steady-state grounding-line positions and their stability for idealized geometries and, in particular, the effect of complete removal of a floating ice shelf on the stability of the grounded ice sheet. For the case where an ice shelf is maintained, buttressing by the shelf may act to stabilize the ice

sheet (for example, Goldberg et al., 2009). The argument is analogous to the mass balance argument of Weertman (1974) and Schoof (2007a). Assuming the calving front of the ice shelf remains stationary, a small retreat of the grounding line would lengthen the ice shelf and increase back pressure at the grounding line, which would lower the stretching rate and thus mass loss across the grounding line.

Studies using numerical flowline models to investigate the stability of marine ice sheets have proven to be inconclusive. The earlier studies of Van der Veen (1985, 1987) suggested that marine ice sheets may be more stable than generally believed and that complete removal of a peripheral ice shelf does not lead to complete disintegration of the ice sheet. Similarly, the model studies of Nick et al. (2010, 2012) indicate that grounding-line dynamics are less sensitive to basal topography as previously suggested and stable grounding-line positions can be attained on a reverse bed slope with or without a floating ice tongue. On the other hand, using a full-Stokes numerical model, Durand et al. (2009a) reaffirmed the assertion that a marine ice sheet is unstable on an upsloping bed. To a large extent, these differences in model behavior may be attributed to how grounding-line dynamics are incorporated and to other numerical specifics.

Vieli and Payne (2005) investigated the ability of numerical flowline models to simulate grounding-line migration in response to changes in accumulation rate and sea level. An important finding is that models that employ a fixed numerical grid show a strong dependency on grid spacing and tend to predict irreversible changes in grounding-line position. In contrast, models that use a moving grid, in which the grounding line always coincides with a grid node, predict smaller changes in grounding-line position, and following a perturbation, a new stable equilibrium is reached. Moreover, the perturbation experiments are reversible, and migration of the grounding line is insensitive to the slope of the bed. A similar influence of grid size on grounding-line dynamics was found by Durand et al. (2009b) using a full Stokes numerical model. Docquier et al. (2011) concluded that for finite-difference models, the numerical implementation has an important effect on grounding-line migration. Models that employ a staggered grid (as in Section 9.3) tend to agree better with the analytical solutions of Schoof (2007a, b) than nonstaggered models, in which velocity and thickness are calculated at the same gridpoints.

The last few years have seen a proliferation of numerical models simulating flow and evolution of marine ice sheets. These models differ in their approximations of the flow of the grounded portion (for example, including gradients in longitudinal stress), boundary conditions at the grounding line (for example, prescribing the ice flux across the grounding line using the Schoof solution), numerics (for example, fixed or moving grid), and other factors. It falls outside the scope of this review to discuss each of these models. For an overview, the reader is referred to Pattyn et al. (2012), who present results of an intercomparison of 27 different flowline models. Validation was provided by comparing model predictions with the analytical solutions of Schoof (2007a, b). Models that are based on lamellar flow for the grounded part fail to reproduce the analytical solutions unless a parameterization of the ice flux across the grounding line is included. Because moving-grid models track movement of the grounding line explicitly, these types of models agreed best with the analytical solutions.

It is important to keep in mind that the marine instability hypothesis essentially consists of two parts, namely, an initial perturbation that initiates grounding-line retreat or advance, and the nonlinear dependency of stretching rate and ice flux across the grounding line on ice thickness, which may cause continued grounding-line migration until a new equilibrium position is reached. On time scales on the order of a decade or so (spanning the period of high spatial and temporal resolution observations on actual outlet glaciers), one favored perturbation is breakup of floating ice shelves or ice tongues and the release of back stress (as in the original model proposed by Mercer, 1968, 1978). Another possible grounding-line perturbation may be increased submarine melting associated with intrusion of relatively warm ocean water under the subshelf cavity (Holland et al., 2008; Motyka et al., 2011).

Observations of rapid changes and large negative mass balances of Greenland and Antarctic outlet glaciers have been well documented using various remote sensing platforms. However, using these observations to identify the physical processes initiating these changes has been hampered by the fact that, typically, multiple changes occur more or less simultaneously—at least at the time resolution at which observations are available—including glacier thinning, flow acceleration, retreat of the calving front, subaqueous melting at or near the grounding line, and increased surface ablation. Nevertheless, a growing consensus appears to be that observed changes in the dynamics of outlet glaciers can be attributed to perturbations at the ice-ocean interface.

Several studies have identified increases in longitudinal stress gradients caused by a large reduction or complete removal of the floating ice tongue as initiating large-scale changes in flow dynamics of bordering outlet glaciers. This view that glacier changes are initiated by an ice-marginal forcing appears to be supported by the observed accelerations of Jakobshavn Isbræ, and Helheim and Kangerdlugssuaq glaciers in Greenland (for example, Howat et al., 2007; Joughin et al., 2008b), Pine Island Glacier in West Antarctica (for example, Payne et al., 2004; Shepherd et al., 2004), and glaciers that used to drain into the Larsen B Ice Shelf prior to its collapse (for example, De Angelis, 2003; Scambos et al., 2004) and elsewhere in the Antarctic Peninsula (for example, Rignot et al., 2004). All of these glaciers underwent changes in the extent of their floating ice tongue, which was coincident with a sudden flow acceleration and glacier thinning. Numerical modeling studies appear to support the notion that release of back stress initiated glacier speedup and thinning (for example, Dupont and Alley, 2005), and further indicate that small changes in the balance of forces at the ice-ocean interface can give rise to velocity increases that are consistent with observations (Payne et al., 2004).

A difficulty with the back-stress model is that, generally, the reduction in back stress at the grounding line is, by itself, not sufficient to affect the stress balance on the grounded part in such a way that rapid accelerations extending several tens of km inland will result. To understand this, consider the force-balance term associated with gradients in longitudinal stress (the second term on the right-hand side of the balance equation (3.22)). Taking the longitudinal stress, R_{xx}, constant with depth, resistance to flow associated with gradients in this stress is given by

$$F_{lon} = -\frac{\partial(H R_{xx})}{\partial x}. \tag{10.97}$$

A decrease in back stress at the grounding line (x = 0) results in an increase in R_{xx} (0) and must be balanced by increased flow resistance on the grounded part because initially the glacier geometry, and thus the driving stress, does not change. Now assume that the increase in stretching stress at the grounding line is instantaneously transmitted over a distance L (the coupling length; Kamb and Echelmeyer, 1986a; Hindmarsh, 2009). Integrating equation (10.97) from x = 0 to x = L gives

$$\int_{0}^{L} F_{lon}\, dx \;=\; H(0)\,R_{xx}(0) \;-\; H(L)\,R_{xx}(L). \qquad (10.98)$$

Averaged over the distance L, resistance associated with gradients in longitudinal stress is then

$$\overline{F}_{lon} \;=\; H(0)\,R_{xx}(0) \;-\; H(L)\,R_{xx}(L). \qquad (10.99)$$

The coupling length represents the distance over which changes in back stress are transmitted upglacier, and $R_{xx}(L)$ remains unchanged, initially. Ignoring for simplicity variations in thickness, the average decrease in $\overline{F}_{lon}$ is then

$$\Delta\overline{F}_{lon} \;=\; \frac{H(0)}{L}\,\Delta R_{xx}(0). \qquad (10.100)$$

Now consider the situation in which the back stress at the grounding line is reduced by 100 kPa. For an ice thickness of 1000 m and using a coupling length of about seven ice thicknesses (Kamb and Echelmeyer, 1986a), this would give an average increase in resistive forces of ~15 kPa. Applying the coupling-length formula derived from scaling principles in Hindmarsh (2009, p. 1755) gives L = 4 km, and the required increase in basal and/or lateral drag is 25 kPa. In the case of Jakobshavn Isbræ, the driving stress ranges from 200 to 400 kPa, and such minor adjustments to resistive stresses appear to be inconsequential and cannot explain the observed doubling of glacier speed (Van der Veen et al., 2011). Note that the above estimate of changes in the role of resistance to flow associated with gradients in longitudinal stress is consistent with the assumption of Schoof (2007a, b) that these stresses are unimportant on the grounded part of a marine ice sheet.

It could be argued that the increase in stretching stress at the grounding line is balanced by a greater increase in resistive stresses, but over a much shorter distance than the coupling length. In that case, resistive stresses upstream of the grounding line would initially not be affected, yet observations on Jakobshavn Isbræ show that changes in glacier speed and stretching stress occurred almost instantaneously over the lower 30–40 km of the glacier. If these changes in speed resulted solely from changes in boundary conditions at the glacier's lower end, one would expect to see a kinematic wave of adjustment traveling upglacier. The force-balance analysis of Van der Veen et al. (2011) indicates that gradients in longitudinal stress remained small and unimportant during the speedup of Jakobshavn Isbræ. Moreover, during

the acceleration, the driving stress did not increase significantly, as would be the case if the upglacier adjustment resulted from steeper slopes migrating inland. Instead, these authors surmise that the velocity changes resulted from weakening of the ice in lateral shear margins and perhaps basal properties. Similarly, the analysis of Joughin et al. (2012) suggests that while loss of buttressing following breakup of the glacier tongue may have contributed to the initial speedup, other processes must have been responsible for continued retreat and speedup of Jakobshavn Isbræ. These authors suggest that thinning-induced changes in the effective basal pressure dominate near-terminus glacier behavior.

Quantitative process studies such as those of Van der Veen et al. (2011) and Joughin et al. (2012) for Jakobshavn Isbræ demonstrate the difficulties faced when interpreting observations. Both weakening of the lateral shear margins (as proposed by Van der Veen et al., 2011) and changes in basal water pressure (Joughin et al., 2012) are plausible explanations for the observed speedup, but additional data to discern between these explanations are currently lacking. Further, the role of confining icebergs and bergy bits in the adjacent fjord on calving rate and the role of ocean melting at the grounding line have yet to be quantified. Consequently, predictions about future behavior of this particular glacier remain fraught with uncertainty.

The conclusions of Van der Veen et al. (2011) and Joughin et al. (2012) regarding possible processes most likely responsible for rapid changes observed on Jakobshavn Isbræ apply to that glacier only and cannot be generalized to other glaciers and to the question of stability of marine ice sheets in general. As pointed out by Truffer and Echelmeyer (2003), a continuum of streaming behavior exists, characterized by different dynamics flow regimes. Jakobshavn Isbræ represents one end member of the spectrum, with high driving stress supported by basal and lateral drag. On the other end of the spectrum are the Siple Coast ice streams moving over very weak beds and with the low, driving stress primarily supported by lateral drag. Stability of these different types of fast-moving glaciers may be entirely different, and concerted quantitative interpretations of data of rapid change pertaining to a range of glaciers, combined with numerical and theoretical modeling, are needed to address the question of stability of marine-terminating glaciers.